

1

2 The ANTsX Ecosystem for Spatiotemporal 3 Mapping of the Mouse Brain

4 Nicholas J. Tustison¹, Min Chen², Fae N. Kronman³, Jeffrey T. Duda², Clare Gamlin⁴,
5 Lydia Ng⁴, Yongsoo Kim³, and James C. Gee²

6 ¹Department of Radiology and Medical Imaging, University of Virginia, Charlottesville, VA

7 ²Department of Radiology, University of Pennsylvania, Philadelphia, PA

8 ³Department of Neural and Behavioral Sciences, Penn State University, Hershey, PA

9 ⁴Allen Institute for Brain Science, Seattle, WA

10

11 Corresponding author:

12 Nicholas J. Tustison, DSc

13 Department of Radiology and Medical Imaging

14 University of Virginia

15 ntustison@virginia.edu

₁₆ **Abstract**

₁₇ Precision mapping techniques coupled with high resolution image acquisition of the mouse
₁₈ brain permit the study of the spatial organization of gene activity and their mutual interac-
₁₉ tion for a comprehensive view of salient structural/functional relationships. Such research
₂₀ is facilitated by standardized anatomical coordinate systems, such as the well-known Allen
₂₁ Common Coordinate Framework version 3 (CCFv3), and the ability to map to such reference
₂₂ atlases. The Advanced Normalization Tools Ecosystem (ANTsX) is a comprehensive open-
₂₃ source software image analysis toolkit, including template building and mapping functional-
₂₄ ity, with applicability to multiple organ systems, modalities, and animal species. Herein, we
₂₅ illustrate the utility of ANTsX for generating precision spatial mappings of the mouse brain
₂₆ of different developmental ages including the prerequisite preprocessing steps. Additionally,
₂₇ as a further illustration of ANTsX capabilities, we use these publicly available mouse brain
₂₈ atlases to generate a velocity flow-based mapping encompassing the entire developmental
₂₉ trajectory, which we also make available to the public.

³⁰ Introduction

³¹ Over the past two decades there have been significant advancements in mesoscopic anal-
³² ysis of the mouse brain. It is now possible to track single cell neurons in 3-D across full
³³ mouse brains,¹ observe whole brain developmental changes on a cellular level,² associate
³⁴ brain regions and tissues with their genetic composition,³ and locally characterize neural
³⁵ connectivity.⁴ Much of this scientific achievement has been made possible due to break-
³⁶ throughs in high resolution imaging techniques that permit submicron, 3-D imaging of whole
³⁷ mouse brains. Associated research techniques such as micro-optical sectioning tomography,⁶
³⁸ tissue clearing,^{1,7} spatial transcriptomics⁹ are all well-utilized in the course of scientific in-
³⁹ vestigations of mesoscale relationships in the mouse brain.

⁴⁰ An important component of this research is the ability to map the various image data to
⁴¹ anatomical reference frames¹¹ for inferring spatial relationships between structures, cells,
⁴² and genetics. This has motivated the development of detailed structural image atlases of the
⁴³ mouse brain. Notable examples include the Allen Brain Atlas and Coordinate Frameworks¹³
⁴⁴ and the Waxholm Space.¹⁴ Despite the significance of these contributions, challenges still
⁴⁵ exist in large part due to the wide heterogeneity in associated study-specific image data. For
⁴⁶ example, variance in the acquisition methods can introduce artifacts such as tissue distor-
⁴⁷ tion, holes, bubbles, folding, tears, and missing slices. These severely complicate assumed
⁴⁸ correspondence for conventional registration approaches.

⁴⁹ To address such challenges, several software packages have been developed over the years
⁵⁰ comprising solutions of varying comprehensibility, sophistication, and availability. An early
⁵¹ contribution to the community was the Rapid Automatic Tissue Segmentation (RATS)
⁵² package¹⁵ for brain extraction which is available upon request. Of the publicly available
⁵³ packages, most, if not all have well-established package dependencies originally developed
⁵⁴ on human brain data. SPMMouse,¹⁶ for example, is based on the well-known Statistical
⁵⁵ Parametric Mapping (SPM) software package.¹⁷ The automated mouse atlas propagation
⁵⁶ (aMAP) tool is largely a front-end for the NiftyReg image registration package¹⁸ applied
⁵⁷ to mouse data which is currently available as a Python module.¹⁹ NiftyReg is also used by
⁵⁸ the Atlas-based Imaging Data Analysis (AIDA) MRI pipeline²⁰ as well as the Multi Atlas

59 Segmentation and Morphometric Analysis Toolkit (MASMAT). Whereas the former also
60 incorporates the FMRIB Software Library (FSL)²¹ for brain extraction and DSISTudio²²
61 for DTI processing, the latter uses NiftySeg and multi-consensus labeling tools²³ for brain
62 extraction and parcellation. In addition, MASMAT incorporates N4 bias field correction²⁴
63 from the Advanced Normalization Tools Ecosystem (ANTsX)²⁵ as do the packages Multi-
64 modal Image Registration And Connectivity anaLysis (MIRACL),²⁶ Saamba-MRI,²⁷ and
65 Small Animal Magnetic Resonance Imaging (SAMRI).²⁸ However, whereas Saamba-MRI uses
66 AFNI²⁹ for image registration; MIRACL, SAMRI, and BrainsMap³⁰ all use ANTsX registra-
67 tion tools. Other packages use landmark-based approaches to image registration including
68 SMART—³¹an R package for semi-automated landmark-based registration and segmenta-
69 tion of mouse brain based on WholeBrain.³² FriendlyClearMap³³ uses the landmark-based
70 registration functionality of Elastix.³⁴ Finally, the widespread adoption of deep learning tech-
71 niques has also influenced development in mouse brain imaging methodologies. For example,
72 if tissue deformations are not considered problematic for a particular dataset, DeepSlice can
73 be used to determine affine mappings³⁵ with the optimal computational efficiency associated
74 with neural networks.

75 The ANTsX Ecosystem

76 As noted above, many of the existing approaches for processing of mouse brain image data
77 use ANTsX tools for core steps in various workflows, particularly its pairwise, intensity-
78 based image registration tools and bias field correction. Historically, ANTsX development
79 is originally based on fundamental approaches to image mapping,^{36–38} particularly in the
80 human brain, which has resulted in core contributions to the field such as the well-known and
81 highly-vetted Symmetric Normalization (SyN) algorithm.³⁹ Since its development, various
82 independent platforms have been used to evaluate ANTsX image registration capabilities in
83 the context of different application foci which include multi-site brain MRI data,⁴⁰ pulmonary
84 CT data,⁴¹ and most recently multi-modal brain registration in the presence of tumors.⁴²
85 Apart from its registration capabilities, ANTsX is a comprehensive biological and medical
86 image analysis toolkit, that comprises additional functionality such as template generation,

Table 1: Sampling of ANTsX functionality

<i>ANTsPy: Preprocessing</i>	
bias field correction	<code>n4_bias_field_correction(...)</code>
image denoising	<code>denoise_image(...)</code>
<i>ANTsPy: Registration</i>	
image registration	<code>registration(...)</code>
template generation	<code>build_template(...)</code>
landmark registration	<code>fit_transform_to_paired_points(...)</code>
time-varying landmark reg.	<code>fit_time_varying_transform_to_point_sets(...)</code>
integrate velocity field	<code>integrate_velocity_field(...)</code>
invert displacement field	<code>invert_displacement_field(...)</code>
<i>ANTsPy: Segmentation</i>	
General segmentation	<code>atropos(...)</code>
Joint label fusion	<code>joint_label_fusion(...)</code>
diffeomorphic thickness	<code>kelly_kapowski(...)</code>
<i>ANTsPy: Miscellaneous</i>	
Regional intensity statistics	<code>label_stats(...)</code>
Regional shape measures	<code>label_geometry_measures(...)</code>
B-spline approximation	<code>fit_bspline_object_to_scattered_data(...)</code>
Visualize images and overlays	<code>plot(...)</code>
<i>ANTsPyNet</i>	
brain extraction	<code>mouse_brain_extraction(...modality="t2"...)</code> <code>mouse_brain_extraction(...modality="ex5"...)</code>
foreground extraction	<code>mouse_histology_brain_mask(...)</code>
midline segmentation	<code>mouse_histology_hemispherical_coronal_mask(...)</code>
cerebellum segmentation	<code>mouse_histology_cerebellum_mask(...)</code>
super resolution	<code>mouse_histology_super_resolution(...)</code>

ANTsX provides state-of-the-art open-science functionality for processing image data. Such tools, including deep learning networks, support a variety of mapping-related tasks. A more comprehensive listing of ANTsX tools with self-contained R and Python examples is provided as a gist page on GitHub (<https://tinyurl.com/antsxtutorial>).

general data approximation, and deep learning networks specifically trained for mouse data (see Table 1). The collective use of the toolkit has demonstrated superb performance in multiple application areas (e.g., consensus labeling,⁴³ brain tumor segmentation,⁴⁴ and cardiac motion estimation).⁴⁵ Importantly, ANTs is built on the Insight Toolkit (ITK)⁴⁶ deriving benefit from a very capable open-source community of scientists and programmers as well as providing a visible, open-source venue for algorithmic contributions.

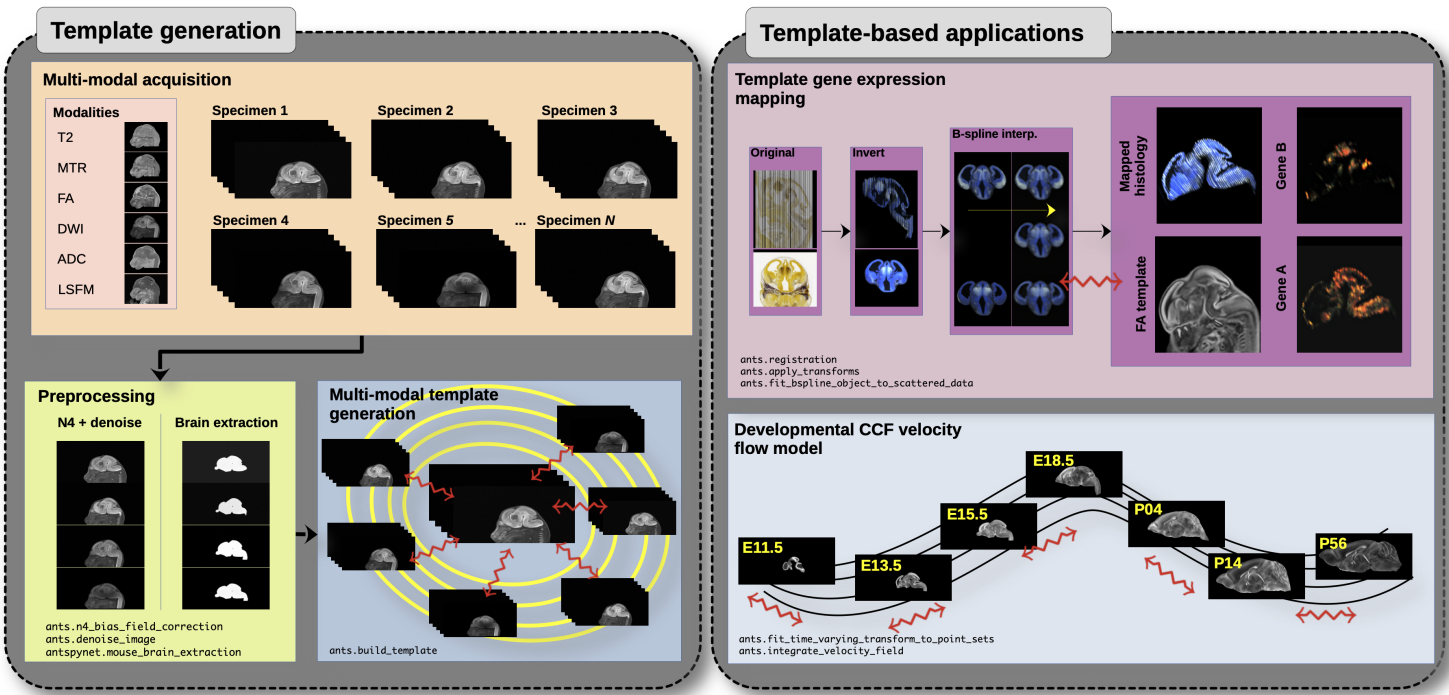


Figure 1: Illustration of a mouse brain template generation workflow and related template-based applications demonstrating the utility of different ANTsX tools. After imaging acquisition of the study population, various preprocessing steps are applied to the imaging data such as bias correction, denoising, and brain extraction as dictated by the needs of the study protocol. In the specific case of the DevCCF, potential applications include gene expression mapping and the generation of the associated velocity flow model for continuous spatiotemporal mapping in the temporal domain spanned by the DevCCF.

Recently, the developmental common coordinate framework (DevCCF) was introduced to the mouse brain research community as a public resource.⁴⁷ These symmetric atlases, comprising both multimodal image data and anatomical segmentations defined by developmental ontology, sample the mouse embryonic days (E) 11.5, E13.5, E15.5, E18.5 and postnatal day (P) 4, P14, and P56. Modalities include at least four MRI contrasts and light sheet fluorescence

98 microscopy (LSFM) per developmental stage. Gene expression and other cell type data were
99 mapped to the corresponding developmental time point to guide the associated anatomical
100 parcellations. The P56 template was integrated with the Allen CCFv3 to further increase
101 the practical utility of the DevCCF. These processes, specifically template generation and
102 multi-modal image mapping, were performed using ANTsX functionality in the presence of
103 previously noted image mapping difficulties (e.g., missing slices, tissue distortion).

104 Given the temporal gaps in the discrete set of developmental atlases with the potential to
105 add additional time points, we discuss the strategy of the current DevCCF template gener-
106 ation described previously⁴⁷ and provide additional information for the interested reader for
107 potential future template generation. Related, we also provide a complementary strategy
108 for inferring correspondence and mapping information within the temporally continuous do-
109 main spanned and sampled by the existing set of embryonic and postnatal atlas brains of the
110 DevCCF. Recently developed ANTsX functionality includes the generation of a diffeomor-
111 phic velocity flow transformation model⁴⁸ spanning developmental stages where mappings
112 between any two continuous time points within the span bounded by the E11.5 and P56
113 atlases is determined by integration of the optimized velocity field.⁴⁹ Such transformations
114 permit the possibility of virtual templates generated between available developmental stages.

₁₁₅ **Results**

₁₁₆ **Template building**

₁₁₇ Template building using ANTsX tools was first described in the context of hippocampal
₁₁₈ studies.⁵⁰ Multi-modal and symmetrical variants were subsequently described as part
₁₁₉ of a proposed brain tumor segmentation approach based on random forests.⁵¹ Tem-
₁₂₀ plate building capabilities are available in both ANTsPy (`ants.build_template(...)`)
₁₂₁ and ANTsR (`buildTemplate(...)`) as well as part of the core ANTs package (e.g.,
₁₂₂ `antsMultivariateTemplateConstruction.sh`).

₁₂₃ **Data preparation**

₁₂₄ Multi-modal symmetric template construction is performed separately for each develop-
₁₂₅ mental stage. Prior to optimization, preprocessing can include several steps not all of
₁₂₆ which are required but are dependent on the data and the particular requirements of the
₁₂₇ study. For MRI scans, inhomogeneity correction is often necessary and can be performed
₁₂₈ using the ANTsPy function `ants.n4_bias_field_correction(...)` which is a wrapper
₁₂₉ for the N4 algorithm.²⁴ Denoising is another preprocessing step that can potentially im-
₁₃₀ prove template quality results. The ANTsPy function `ants.denoise_image(...)` is an
₁₃₁ implementation of a well-known denoising algorithm.⁵² For a typical image, both of these
₁₃₂ steps takes approximately on the order of a couple minutes. In ANTsX, due to legacy
₁₃₃ code issues, only bias correction is wrapped with template building so one need not per-
₁₃₄ form this step prior to optimization. In addition, brain extraction has demonstrated im-
₁₃₅ proved performance in the context of human brain normalization⁵³ and is similarly used
₁₃₆ in mouse brain registration to maximize alignment. Various approaches within ANTs are
₁₃₇ possible including a template-based approach `antsBrainExtraction.sh` or using deep learn-
₁₃₈ ing `antspynet.mouse_brain_extraction(...)`. Additionally, it is important to ensure a
₁₃₉ standardized orientation, similar to the Dicom standard for human brain imaging. A study
₁₄₀ requirement of template bilateral symmetry is also an important consideration prior to tem-
₁₄₁ plate generation. This can be performed by either flipping all the input images contralaterally

142 such that all input specimens are represented twice or one can generate an initial asymmetric
143 template, flipping it contralaterally, and using the two asymmetric templates in a subsequent
144 template generation call to create a single symmetric template. For multi-modal templates,
145 all the images for a single specimen need to be mutually aligned in the same image space
146 prior to optimization. After selecting the target image space for a particular specimen
147 (e.g., T2-weighted MRI), this can be performed with a rigid transform registration call us-
148 ing `ants.registration(...)`. It should be noted that for most applications, the general
149 heuristic of ≈ 10 randomly sampled specimens is sufficient for a satisfactory template.

150 In the case of the DevCCF, bias correction was employed in generating the multiple stage
151 templates using the shell script `antsMultivariateConstruction.sh`. Brain extraction was
152 applied to the postnatal images. Template symmetrization employed the original and con-
153 tralateral versions of all specimen images.

154 Optimization

155 Template generation is initialized with either a user-provided image or a bootstrapped ini-
156 tialization template constructed from the input data. If the latter is selected, the voxelwise
157 averaged image for each modality is constructed followed by a linear registration of each
158 specimen to this template initialization which refines the estimate. The former option is
159 often used where computational considerations are important. For example, this initial tem-
160 plate can be generated using low resolution input data or only a subset of the input cohort.
161 This higher quality initial estimate can then be further refined using the entire data set at
162 full resolution.

163 Following template initialization, each specimen is registered to the current template es-
164 timate, which can be performed in parallel. After the current round of registrations is
165 complete, a voxelwise average of each modality is performed with optional Laplacian sharp-
166 ening followed by a “shape update” step. This shape update step is used to warp the current
167 estimate of the template so that its shape is closer to the mean shape of the input data.
168 Implementation-wise this is done by averaging each displacement field that points from the
169 template to the affinely warped specimen. This average displacement field is then used to

170 deform the voxelwise-averaged template. Shape and intensity template convergence typically
171 occurs in four deformable iterations.

172 The DevCCF Velocity Flow Model

173 To continuously link the DevCCF atlases, a velocity flow model was constructed using Dev-
174 CCF derived data and ANTsX functionality available in both ANTsR and ANTsPy. Al-
175 though many implementations optimize variations of this transformation model (and others)
176 using various image intensity similarity metrics, we opted to implement a separate de-
177 termination of iterative correspondence and transformation optimization. This decision was
178 based on existing ANTsX functionality and wanting complementary utility for the toolkit.

179 ANTsX, being built on top of ITK, uses an ITK image data structure for the 4-D velocity
180 field where each voxel contains the x , y , z components of the field at that point. Field
181 regularization is provided by a novel B-spline scattered data approximation technique⁵⁴ which
182 permits individual point-based weighting. Both field regularization and integration of the
183 velocity field are built on ITK functions written by ANTsX developers.

184 The optimized velocity field described here is of size [256, 182, 360] ($50\mu\text{m}$ isotropic) \times 11
185 integration points for a total compressed size of a little over 2 GB. This choice represented
186 weighing the trade-off between tractability, portability, and accuracy. However, all data
187 and code to reproduce the results described are available in a dedicated GitHub repository
188 (<https://github.com/ntustison/DevCCF-Velocity-Flow>).

189 Data preparation

190 Labeled annotations are available as part of the original DevCCF and reside in the space
191 of each developmental template which range in resolution from $31.5 - 50\mu\text{m}$. Across all at-
192 lases, the total number of labels exceeded 2500 without taken into account per hemispherical
193 enumeration. From this set of labels, there were a common set of 24 labels (12 per hemi-
194 sphere) across all atlases that were used for optimization and evaluation. These regions are
195 illustrated for the P4 and P14 stages in Figure 2.

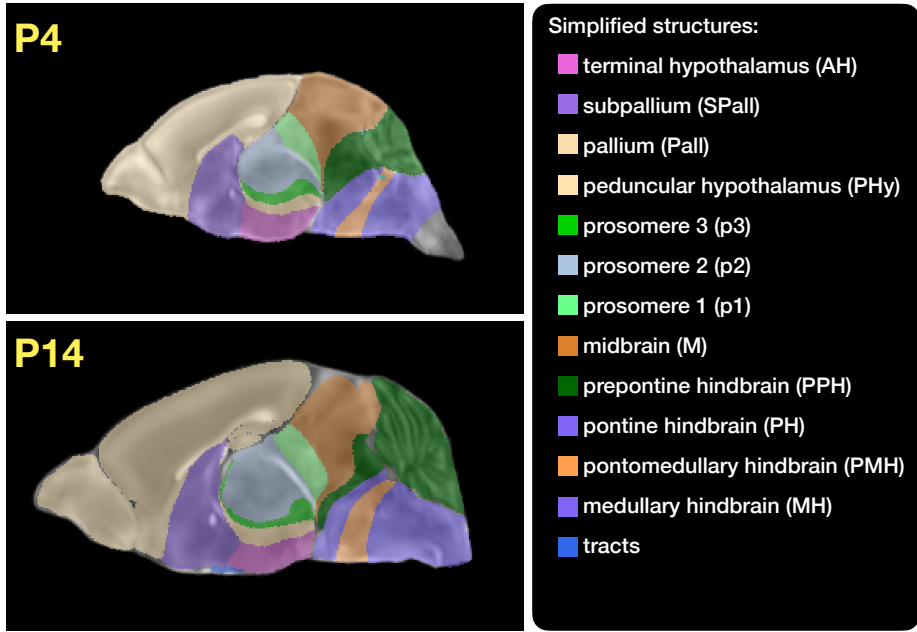


Figure 2: Annotated regions representing common labels across developmental stages which are illustrated for both P4 and P14.

Prior to velocity field optimization, the data was rigidly transformed to a common space. Using the centroids for the common label set of each CCFDev atlas, the ANTsPy `ants.fit_transform_to_paired_points(...)` function was used to warp each atlas to the space of the P56 atlas and then downsampled to $50\mu\text{m}$ isotropic resolution. In order to determine the common point sets across stages, the multi-metric capabilities of `ants.registration(...)` were used. Instead of performing intensity-based pairwise registration directly on these multi-label images, each label was used to construct a separate fixed and moving image pair resulting in a multi-metric registration optimization scenario involving 24 binary image pairs (each label weighted equally) for optimizing correspondence between neighboring atlases using the mean squares metric and the SyN transform.

To provide the common point sets across all seven developmental atlases, the label boundaries and whole regions were sampled in the P56 atlas and then propagated to each atlas using the transformations derived from the pairwise registrations. Based on previous experience as both the developers of users of these tools, we selected a sampling rate of 10% for the contour points and 1% for the regional points for a total number of points being per atlas being 173303 ($N_{contour} = 98151$ and $N_{region} = 75152$). Boundary points were weighted twice

as those of regional points for the B-spline data approximation optimization.

Optimization

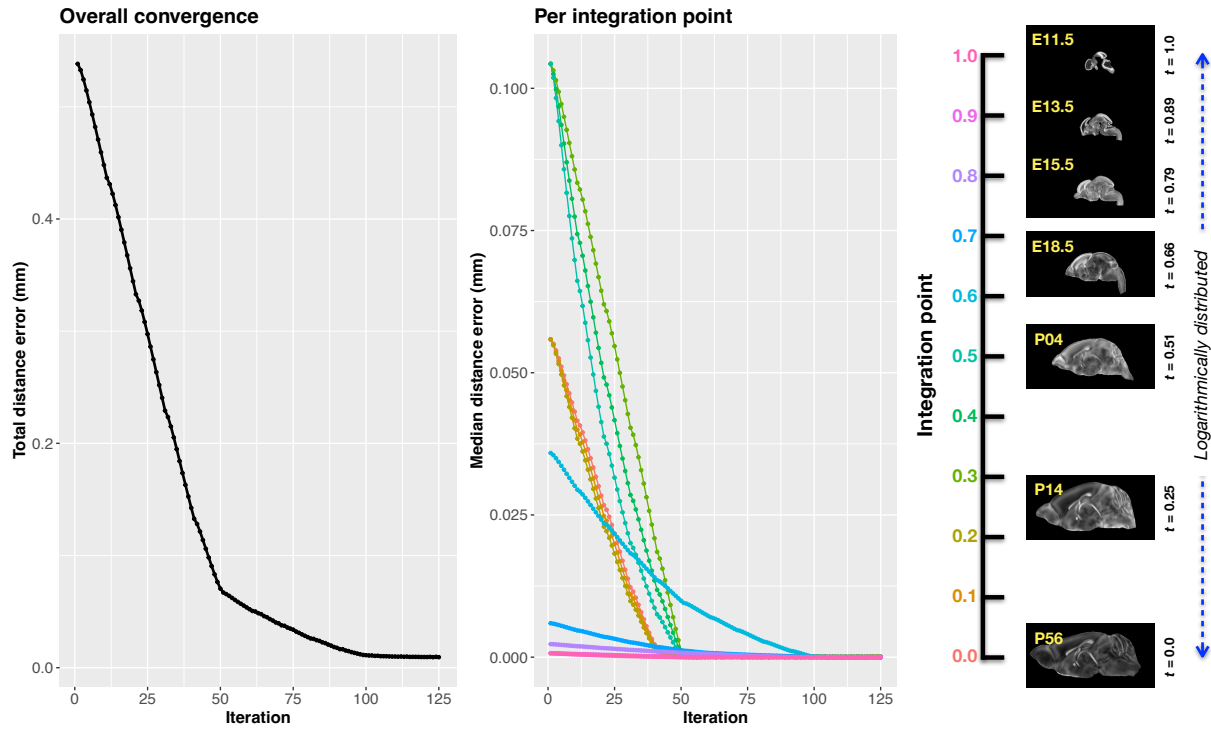


Figure 3: Convergence of the optimization of the velocity field for describing the transformation through the developmental stages from E11.5 through P56.

`ants.fit_time_varying_transform_to_point_sets(...)` from the ANTsPy package was used to optimize the velocity field. Input comprised the seven corresponding point sets and their associated weight values, the selected number of integration points for the velocity field ($N = 11$), and the parameters defining the geometry of the spatial dimensions of the velocity field (same as the downsampled P56 atlas noted above). In addition, the normalized time point for each atlas/point-set was also defined. Given the increasingly larger gaps in the postnatal timepoint sampling, we made two adjustments. Based on known mouse brain development, we used 28 days for the P56 data. We then computed the log transform of the adjusted set of time points prior to normalization between 0 and 1 (see the right side of Figure 3.) This log transform, as part of the temporal normalization, significantly improved data spacing.

225 The max number of iterations was set to 200. At each iteration we looped over the 11
 226 integration points. At each integration point, the velocity field estimate was updated by
 227 warping the two immediately adjacent point sets to the integration time point and deter-
 228 mining the regularized displacement field between the two warped point sets. As with any
 229 gradient-based descent algorithm, this field was multiplied by a small step size ($\delta = 0.2$)
 230 before adding to the current velocity field. Using multithreading, each iteration took about
 231 six minutes.

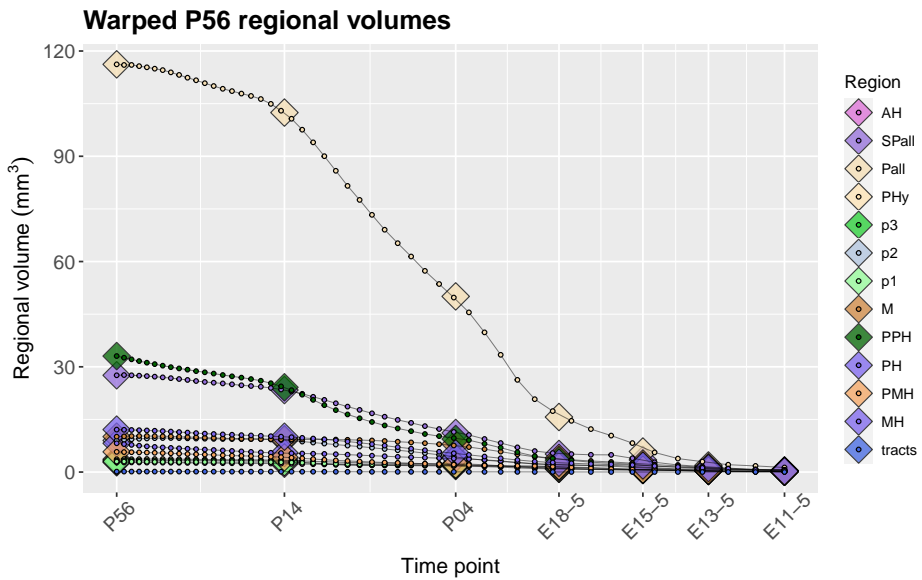


Figure 4: After the velocity field is generated, we can use it to warp the simplified labels of the P56 atlas continuously over the interval [0, 1] and plot the volumes of the atlas regions. Note how they compare with the volumes of the same regions in the other atlases.

232 Convergence is determined by the average displacement error over each of the integration
 233 points. As can be seen in the left panel of Figure 3, convergence occurred around 125
 234 iterations when the average displacement error is minimized. The median displacement
 235 error at each of the integration points also trends towards zero but at different rates. After
 236 optimization, we use the velocity field to warp the P56 set of labels to each of the other atlas
 237 time points to compare the volumes of the different simplified annotated regions. This is
 238 shown in Figure 4.

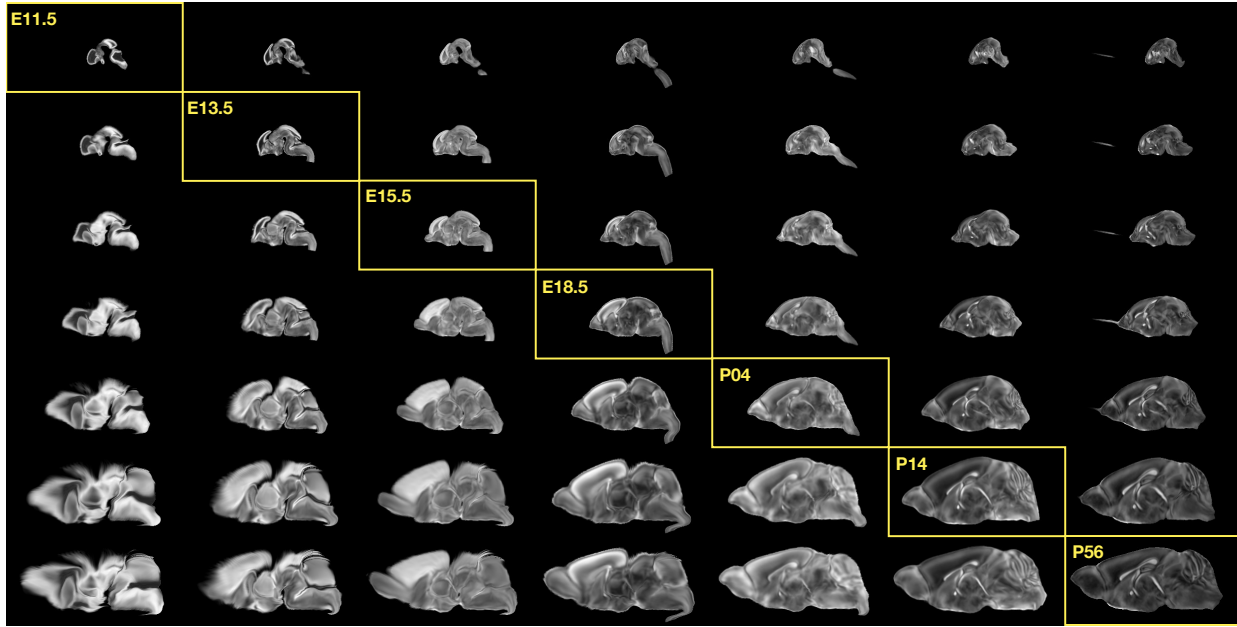


Figure 5: Mid-sagittal visualization of the effects of the transformation model in warping every developmental stage to the time point of every other developmental stage. The original images are located along the diagonal. Columns correspond to the warped original image whereas the rows represent the reference space to which each image is warped.

239 The DevCCF transform model

240 Once optimized, the resulting velocity field can be used to generate the deformable transform
241 between any two continuous points within the time interval bounded by E11.5 and P56. So,
242 for example, one can transform each atlas to the space of every other atlas. This is illustrated
243 in Figure 5 where we render a mid-sagittal location for each atlas and the results of warping
244 every atlas to that space.

245 One potential application for this particular transformation model is facilitating the con-
246 struction of virtual-templates in the temporal gaps of the DevCCF. This is illustrated in
247 Figure 6 where we used the optimized velocity field to construct virtual-templates at time
248 point P10.3 and P20—arbitrarily chosen simply to demonstrate the concept. After situating
249 these time points within the normalized time point interval, the existing adjacent DevCCF
250 atlases on either side can be warped to the desired time point. A subsequent call to one
251 of the ANTsX template building functions then permits the construction of the template
252 at that time point. Note that both of these usage examples can be found on the GitHub

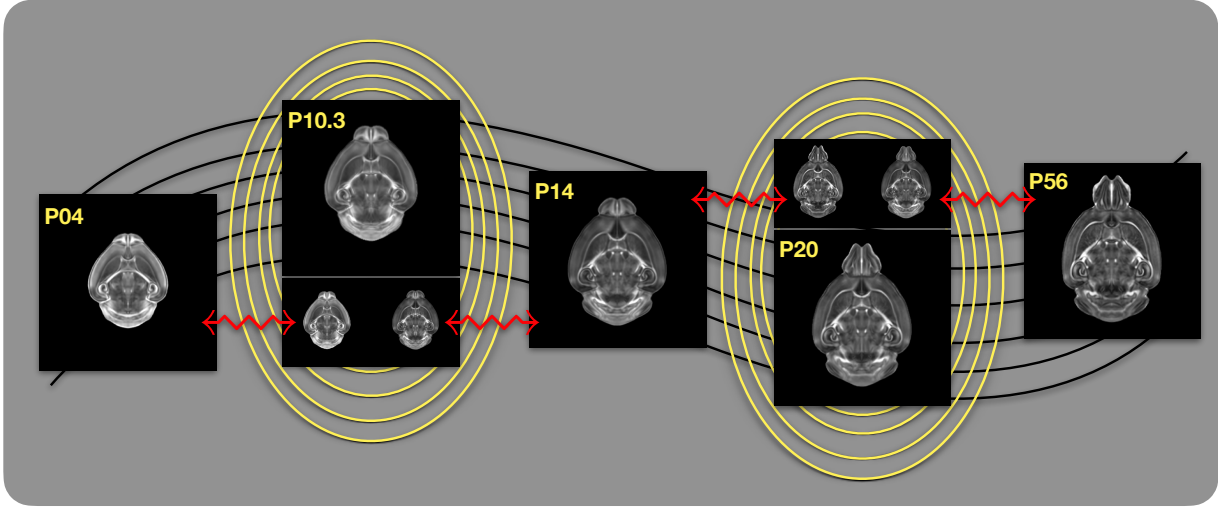


Figure 6: Illustration of the use of the velocity flow model for creating virtual templates at continuous time points not represented in one of the existing DevCCF time points. For example, FA templates at time point P10.3 and P20 can be generated by warping the existing temporally adjacent developmental templates to the target time point and using those images in the ANTsX template building process.

²⁵³ repository given above.

254 **Discussion**

255 The ANTsX ecosystem is a powerful framework that has demonstrated
256 applicability to multiple species and organ systems, including the mouse brain.
257 This has been demonstrated in many ways including the significant number of external
258 software packages that use various ANTsX components in their own mouse-specific work-
259 flows. The extensive functionality of ANTsX makes it possible to create complete processing
260 pipelines without requiring multiple packages which often have limited cross-compatibility
261 evaluation.

262 These open-source ANTsX components not only perform well but are available across mul-
263 tiple popular platforms (e.g., R and Python) which facilitates the construction of tailored
264 pipelines for individual study solutions. These components are also supported by years of
265 development not only by the ANTsX development team but by the larger ITK community.

266 In the case of the development of the DevCCF, ANTsX was crucial in providing necessary
267 functionality for yielding high quality output. First, for the generation of the individual
268 developmental stage multi-modal, symmetric templates, ANTsX is unique amongst image
269 analysis software packages in providing existing solutions for template generation which have
270 been vetted, including being used in several studies over the years, and which continue to be
271 under active refinement. At its core, computationally efficient and quality template gener-
272 ation requires the use of precision pairwise image mapping functionality which, historically,
273 is at the origins of the ANTsX ecosystem. And these mapping capabilities extend beyond
274 template generation to the mapping of other image data (e.g., gene expression maps) to
275 template for providing further insight into the mouse brain.

276 Despite the significant expansion of available developmental age templates beyond what pre-
277 viously existed (e.g., Allen CCFv3), there still exist temporal gaps in the DevCCF. However,
278 pioneering work involving diffeomorphic transformations allowed us to continuously situate
279 the existing templates within a time-varying velocity flow model. This allows one to deter-
280 mine the diffeomorphic transformation from any one temporal location to any other temporal
281 location within the time span defined by the E11.5 and P56 templates. This functionality
282 is built on multiple components from the Insight Segmentation and Registratiton Toolkit

283 including the B-spline scattered data approximation technique for field regularization and
284 velocity field integration using fourth order Runge-Kutta. This velocity field model permits
285 intra-template comparison and the construction of virtual templates where a template can
286 be estimated at any continuous time point within the temporal domain. This novel appli-
287 cation can potentially enhance our understanding of intermediate developmental states. To
288 increase its impact and reproduce the results shown previously, we have made the data and
289 code publicly available at <https://github.com/ntustison/DevCCF-Velocity-Flow>.

290 Although ANTsX is quite evolved in its development and functionality, there are several
291 areas which are currently under active development or consideration for further expan-
292 sion. Most notably, as in our human applications, deep learning has had a significant
293 impact in steering our attention. Core functionality, such as brain extraction for mouse
294 brain mapping, would benefit from increasing the number of available modalities. As with
295 much deep learning development, such work will require additional data but is significantly
296 facilitated by the tools that we have created in both ANTsPyNet and ANTsRNet. Re-
297 lated would be the utility of the development of mouse brain parcellation tools such as our
298 `antspynet.desikan_killiany_tourville_labeling(...)` tool.

²⁹⁹ **Methods**

³⁰⁰ The following methods are all available as part of the ANTsX ecosystem with analogous
³⁰¹ elements existing in both ANTsR (ANTs in R) and ANTsPy (ANTs in Python) with and
³⁰² ANTs/ITK C++ core. However, most of the development for the work described below was
³⁰³ performed using ANTsPy. For equivalent calls in ANTsR, please see the ANTsX tutorial at
³⁰⁴ <https://tinyurl.com/antsxtutorial>.

³⁰⁵ **Preprocessing: bias field correction and denoising**

³⁰⁶ As in human studies, bias field correction and image denoising are standard preprocessing
³⁰⁷ steps in improving overall image quality in mouse brain images. The bias field, a gradual
³⁰⁸ spatial intensity variation in images, can arise from various sources such as magnetic field in-
³⁰⁹ homogeneity or acquisition artifacts, leading to distortions that can compromise the quality
³¹⁰ of brain images. Correcting for bias fields ensures a more uniform and consistent representa-
³¹¹ tion of brain structures, enabling accurate quantitative analysis. Additionally, brain images
³¹² are often susceptible to various forms of noise, which can obscure subtle features and affect
³¹³ the precision of measurements. Denoising techniques help mitigate the impact of noise, en-
³¹⁴ hancing the signal-to-noise ratio and improving the overall image quality. The well-known
³¹⁵ N4 bias field correction algorithm²⁴ has its origins in the ANTs toolkit which was imple-
³¹⁶ mented and introduced into the ITK toolkit. Similarly, ANTsX contains an implementation
³¹⁷ of a well-performing patch-based denoising technique⁵² and is also available as a image filter
³¹⁸ to the ITK community.

³¹⁹ **ANTsXNet mouse brain applications**

³²⁰ *General notes regarding deep learning training.*

³²¹ All network-based approaches described below were implemented and organized in the
³²² ANTsXNet libraries comprising Python (ANTsPyNet) and R (ANTsRNet) analogs using the
³²³ Keras/Tensorflow libraries available as open-source in ANTsX GitHub repositories. For the

324 various applications, both share the identically trained weights for mutual reproducibility.
325 Training data was provided by manual labeling by various co-authors and expanded using
326 both intensity-based and shape-based data augmentation techniques.

327 Intensity-based data augmentation consisted of randomly added noise based on
328 ITK functionality, simulated bias fields based on N4 bias field modeling, and his-
329 togram warping for mimicking well-known MRI intensity nonlinearities.^{25,55} These
330 augmentation techniques are available in ANTsXNet (only ANTsPyNet versions are
331 listed): simulated bias field: `antspynet.simulate_bias_field(...)`, image noise:
332 `antspyhet.add_noise_to_image(...)`, and MRI intensity nonlinear characteriza-
333 tion: `antspynet.histogram_warp_image_intensities(...)`. Shape-based data
334 augmentation used both random linear and nonlinear deformations. This func-
335 tionality is also instantiated within ANTsXNet in terms of random spatial warping:
336 `antspynet.randomly_transform_image_data(...)`.

337 For all GPU training, we used Python scripts for creating custom batch generators. As such
338 batch generators tend to be application-specific, we store them in a separate GitHub reposi-
339 tory for public availability (<https://github.com/ntustison/ANTsXNetTraining>). In terms of
340 GPU hardware, all training was done on a DGX (GPUs: 4X Tesla V100, system memory:
341 256 GB LRDIMM DDR4).

342 *Brain extraction.*

343 Similar to human neuroimage processing, brain extraction is a crucial preprocessing step for
344 accurate brain mapping. Within ANTsXNet, we have created several deep learning networks
345 for brain extraction for several image modalities (e.g., T1, FLAIR, fractional anisotropy).
346 Similarly, for the developmental brain atlas work⁴⁷ we developed similar functionality for
347 mouse brains of different modalities and developmental age. All networks use a conven-
348 tional 2-D U-net architecture⁵⁶ and perform prediction in a slice-wise fashion given the
349 limitations of the acquisition protocols (e.g., missing slices, slice thickness). Currently,
350 coronal and sagittal networks are available for both E13.5 and E15.5 data and coronal
351 network for T2-weighted MRI. In ANTsPyNet, this functionality is available in the pro-
352 gram `antspynet.mouse_brain_extraction(...)`. Even when physical brain extraction is

³⁵³ performed prior to image acquisition, artifacts, such as bubbles or debris, can complicate
³⁵⁴ subsequent processing. Similar to the brain extraction networks, a 2-D U-net architecture⁵⁶
³⁵⁵ was created to separate the background and foreground.

³⁵⁶ *Miscellaneous networks: Super-resolution, cerebellum, and hemispherical masking.*

³⁵⁷ To further enhance the data prior to designing mapping protocols, additional networks were
³⁵⁸ created. A well-performing deep back projection network⁵⁷ was ported to ANTsXNet and
³⁵⁹ expanded to 3-D for various super-resolution applications,⁵⁸ including mouse data. Finally,
³⁶⁰ features of anatomical significance, namely the cerebellum and hemispherical midline were
³⁶¹ captured in these data using deep learning networks.

³⁶² **Intra-slice image registration with missing slice imputation**

³⁶³ Volumetric gene expression slice data was collated into 3-D volumes using ... (ask Jeff).
³⁶⁴ Prior to mapping this volume to the corresponding structural data and, potentially, to the
³⁶⁵ appropriate template, alignment was improved using deformable registration on contiguous
³⁶⁶ slices. However, one of the complications associated with these image data was the un-
³⁶⁷ known number of missing slices, the number of consecutive missing slices, and the different
³⁶⁸ locations of these missing slices. To handle this missing data problem, we found that data
³⁶⁹ interpolation using the B-spline approximation algorithm cited earlier⁵⁴ (ANTsPy function:
³⁷⁰ `ants.fit_bspline_object_to_scattered_data(...)`). This provided sufficient data in-
³⁷¹ terpolation fidelity to perform continuous slicewise registration. Other possible variants that
³⁷² were considered but deemed unnecessary was performing more than one iteration cycling
³⁷³ through data interpolation and slicewise alignment. The other possibility was incorporating
³⁷⁴ the super-resolution technique described earlier. But again, our data did not require these
³⁷⁵ additional steps.

³⁷⁶ **Image registration**

³⁷⁷ The ANTs registration toolkit is a complex framework permitting highly tailored so-
³⁷⁸ lutions to pairwise image registration scenarios.⁵⁹ It includes innovative transformation

³⁷⁹ models for biological modeling^{39,60} and has proven capable of excellent performance.^{40,61}
³⁸⁰ Various parameter sets targeting specific applications have been packaged with the
³⁸¹ different ANTsX platforms, specifically ANTs, ANTsPy, and ANTsR.²⁵ In ANTsPy,
³⁸² the function `ants.registration(...)` is used to register two (sets) of images where
³⁸³ `type_of_transform` is a user-specified option that invokes a specific parameter set. For
³⁸⁴ example `type_of_transform='antsRegistrationSyNQuick[s]'` is an oft-used parameter
³⁸⁵ set.

³⁸⁶ Initially, linear optimization is initialized with center of (intensity) mass alignment typically
³⁸⁷ followed by optimization of both rigid and affine transforms using the mutual information
³⁸⁸ similarity metric. This was followed by diffeomorphic deformable alignment using symmetric
³⁸⁹ normalization (SyN) with Gaussian³⁹ or B-spline regularization⁶⁰ where the forward trans-
³⁹⁰ form is invertible and differentiable. The similarity metric employed at this latter stage is
³⁹¹ typically either neighborhood cross-correlation or mutual information similarity metric. Note
³⁹² that these parameter sets are robust to input image type (i.e., LSFM, Nissl staining, and the
³⁹³ various MRI modalities) and are adapatable to mousing image geometry scaling. Further
³⁹⁴ details can be found in the various documentation sources for these ANTsX packages.

³⁹⁵ **Template generation**

³⁹⁶ ANTsX provides functionality for constructing templates from a set (or multi-modal sets) of
³⁹⁷ input images as originally described⁵⁰ and recently used to create the DevCCF templates.⁴⁷
³⁹⁸ An initial template estimate is constructed from an existing subject image or a voxelwise
³⁹⁹ average derived from a rigid pre-alignment of the image population. Pairwise registration
⁴⁰⁰ between each subject and the current template estimate is performed using the Symmetric
⁴⁰¹ Normalization (SyN) algorithm.³⁹ The template estimate is updated by warping all subjects
⁴⁰² to the space of the template, performing a voxelwise average, and then performing a “shape
⁴⁰³ update” of this latter image by warping it by the average inverse deformation, thus yielding
⁴⁰⁴ a mean image of the population in terms of both the intensity and shape.

405 **Continuous developmental velocity flow transformation model**

406 Given multiple, linearly or non-linearly ordered point sets where individual points across
407 are in one-to-one correspondence, we developed an approach for generating a velocity flow
408 transformation model to describe a time-varying diffeomorphic mapping as a variant of the
409 inexact landmark matching solution of Joshi and Miller.⁴⁸ Integration of the resulting velocity
410 field can then be used to describe the displacement between any two time points within this
411 time-parameterized domain. Regularization of the sparse correspondence between point sets
412 is performed using a generalized B-spline scattered data approximation technique,⁵⁴ also
413 developed by the ANTsX developers and contributed to ITK.

414 To apply this methodology to the developmental templates,⁴⁷ we coalesced the manual par-
415 cellations of the developmental templates into 26 common anatomical regions (13 per hemi-
416 sphere). We then used these regions to generate invertible transformations between succe-
417 ssive time points. Specifically each label was used to create a pair of single region images
418 resulting in 26 pairs of “source” and “target” images. The multiple image pairs were used
419 to iteratively estimate a diffeomorphic pairwise transform. Given the seven atlases E11.5,
420 E13.5, E15.5, E18.5, P4, P14, and P56, this resulted in 6 sets of transforms between succe-
421 ssive time points. Given the relative sizes between atlases, on the order of 10^6 points were
422 randomly sampled labelwise in the P56 template space and propagated to each successive
423 atlas providing the point sets for constructing the velocity flow model. Approximately 200
424 iterations resulted in a steady convergence based on the average Euclidean norm between
425 transformed point sets. Ten integration points were used and point sets were distributed
426 along the temporal dimension using a log transform for a more evenly spaced sampling.
427 Further details including links to data and scripts to reproduce our reported results is found
428 in the associated GitHub repository.

429 **Visualization**

430 To complement the well-known visualization capabilities of R and Python, e.g., ggplot2
431 and matplotlib, respectively, image-specific visualization capabilities are available in the

432 `ants.plot(...)` (Python) and `plot.antsImage(...)` (R). These are capable of illustrating
433 multiple slices in different orientations with both other image overlays as well as label images.

434 **Data availability.** All data used in this work are publicly available. The DevCCF atlas is
435 available at <https://kimlab.io/brain-map/DevCCF/>. Additionally, all software discussed is
436 publicly available. ANTsPy and ANTsR are available through GitHub at the ANTsX Ecosys-
437 tem (<https://github.com/ANTsX>). A GitHub repository specific to the work discussed in the
438 manuscript was created and is available at <https://github.com/ntustison/DevCCF-Velocity->
439 **Flow.**

440 **References**

- 441 1. Keller, P. J. & Ahrens, M. B. Visualizing whole-brain activity and development at
442 the single-cell level using light-sheet microscopy. *Neuron* **85**, 462–83 (2015).
- 443 2. La Manno, G. *et al.* Molecular architecture of the developing mouse brain. *Nature*
444 **596**, 92–96 (2021).
- 445 3. Wen, L. *et al.* Single-cell technologies: From research to application. *Innovation*
446 (*Camb*) **3**, 100342 (2022).
- 447 4. Oh, S. W. *et al.* A mesoscale connectome of the mouse brain. *Nature* **508**, 207–14
448 (2014).
- 449 5. Gong, H. *et al.* Continuously tracing brain-wide long-distance axonal projections in
450 mice at a one-micron voxel resolution. *Neuroimage* **74**, 87–98 (2013).
- 451 6. Li, A. *et al.* Micro-optical sectioning tomography to obtain a high-resolution atlas of
452 the mouse brain. *Science* **330**, 1404–8 (2010).
- 453 7. Ueda, H. R. *et al.* Tissue clearing and its applications in neuroscience. *Nat Rev*
454 *Neurosci* **21**, 61–79 (2020).
- 455 8. Ståhl, P. L. *et al.* Visualization and analysis of gene expression in tissue sections by
456 spatial transcriptomics. *Science* **353**, 78–82 (2016).
- 457 9. Burgess, D. J. Spatial transcriptomics coming of age. *Nat Rev Genet* **20**, 317 (2019).
458
- 459 10. MacKenzie-Graham, A. *et al.* A multimodal, multidimensional atlas of the C57BL/6J
460 mouse brain. *J Anat* **204**, 93–102 (2004).
- 461 11. Mackenzie-Graham, A. J. *et al.* Multimodal, multidimensional models of mouse brain.
462 *Epilepsia* **48 Suppl 4**, 75–81 (2007).
- 463 12. Dong, H. W. *Allen reference atlas. A digital color brain atlas of the C57BL/6J male*
464 *mouse.* (John Wiley; Sons, 2008).

- 465 13. Wang, Q. *et al.* The allen mouse brain common coordinate framework: A 3D reference
466 atlas. *Cell* **181**, 936–953.e20 (2020).
- 467 14. Johnson, G. A. *et al.* Waxholm space: An image-based reference for coordinating
468 mouse brain research. *Neuroimage* **53**, 365–72 (2010).
- 469 15. Oguz, I., Zhang, H., Rumple, A. & Sonka, M. RATS: Rapid automatic tissue segmen-
470 tation in rodent brain MRI. *J Neurosci Methods* **221**, 175–82 (2014).
- 471 16. Sawiak, S. J., Picq, J.-L. & Dhenain, M. Voxel-based morphometry analyses of in
472 vivo MRI in the aging mouse lemur primate. *Front Aging Neurosci* **6**, 82 (2014).
- 473 17. Ashburner, J. SPM: A history. *Neuroimage* **62**, 791–800 (2012).
- 474
- 475 18. Modat, M. *et al.* Fast free-form deformation using graphics processing units. *Comput
476 Methods Programs Biomed* **98**, 278–84 (2010).
- 477 19. Tyson, A. L. *et al.* Accurate determination of marker location within whole-brain
478 microscopy images. *Sci Rep* **12**, 867 (2022).
- 479 20. Pallast, N. *et al.* Processing pipeline for atlas-based imaging data analysis of struc-
480 tural and functional mouse brain MRI (AIDAmri). *Front Neuroinform* **13**, 42 (2019).
- 481 21. Jenkinson, M., Beckmann, C. F., Behrens, T. E. J., Woolrich, M. W. & Smith, S. M.
482 FSL. *Neuroimage* **62**, 782–90 (2012).
- 483 22. Yeh, F.-C., Wedeen, V. J. & Tseng, W.-Y. I. Generalized q-sampling imaging. *IEEE
484 Trans Med Imaging* **29**, 1626–35 (2010).
- 485 23. Jorge Cardoso, M. *et al.* STEPS: Similarity and truth estimation for propagated
486 segmentations and its application to hippocampal segmentation and brain parcelation.
Med Image Anal **17**, 671–84 (2013).
- 487 24. Tustison, N. J. *et al.* N4ITK: Improved N3 bias correction. *IEEE Trans Med Imaging*
488 **29**, 1310–20 (2010).

- 489 25. Tustison, N. J. *et al.* The ANTsX ecosystem for quantitative biological and medical
490 imaging. *Sci Rep* **11**, 9068 (2021).
- 491 26. Goubran, M. *et al.* Multimodal image registration and connectivity analysis for inte-
492 gration of connectomic data from microscopy to MRI. *Nat Commun* **10**, 5504 (2019).
- 493 27. Celestine, M., Nadkarni, N. A., Garin, C. M., Bougacha, S. & Dhenain, M. Sammba-
494 MRI: A library for processing SmAll-MaMmal BrAin MRI data in python. *Front
Neuroinform* **14**, 24 (2020).
- 495 28. Ioanas, H.-I., Marks, M., Zerbi, V., Yanik, M. F. & Rudin, M. An optimized regis-
496 tration workflow and standard geometric space for small animal brain imaging. *Neu-
roimage* **241**, 118386 (2021).
- 497 29. Cox, R. W. AFNI: What a long strange trip it's been. *Neuroimage* **62**, 743–7 (2012).
- 498
- 499 30. Ni, H. *et al.* A robust image registration interface for large volume brain atlas. *Sci
500 Rep* **10**, 2139 (2020).
- 501 31. Jin, M. *et al.* SMART: An open-source extension of WholeBrain for intact mouse
502 brain registration and segmentation. *eNeuro* **9**, (2022).
- 503 32. Fürth, D. *et al.* An interactive framework for whole-brain maps at cellular resolution.
504 *Nat Neurosci* **21**, 139–149 (2018).
- 505 33. Negwer, M. *et al.* FriendlyClearMap: An optimized toolkit for mouse brain mapping
506 and analysis. *Gigascience* **12**, (2022).
- 507 34. Klein, S., Staring, M., Murphy, K., Viergever, M. A. & Pluim, J. P. W. Elastix: A
508 toolbox for intensity-based medical image registration. *IEEE Trans Med Imaging* **29**,
196–205 (2010).
- 509 35. Carey, H. *et al.* DeepSlice: Rapid fully automatic registration of mouse brain imaging
510 to a volumetric atlas. *Nat Commun* **14**, 5884 (2023).

- 511 36. Bajcsy, R. & Broit, C. Matching of deformed images. in *Sixth International Conference on Pattern Recognition (ICPR'82)* 351–353 (1982).
- 512
- 513 37. Bajcsy, R. & Kovacic, S. Multiresolution elastic matching. *Computer Vision, Graphics, and Image Processing* **46**, 1–21 (1989).
- 514
- 515 38. Gee, J., Sundaram, T., Hasegawa, I., Uematsu, H. & Hatabu, H. Characterization of regional pulmonary mechanics from serial magnetic resonance imaging data. *Acad Radiol* **10**, 1147–52 (2003).
- 516
- 517 39. Avants, B. B., Epstein, C. L., Grossman, M. & Gee, J. C. Symmetric diffeomorphic image registration with cross-correlation: Evaluating automated labeling of elderly and neurodegenerative brain. *Med Image Anal* **12**, 26–41 (2008).
- 518
- 519 40. Klein, A. *et al.* Evaluation of 14 nonlinear deformation algorithms applied to human brain MRI registration. *Neuroimage* **46**, 786–802 (2009).
- 520
- 521 41. Murphy, K. *et al.* Evaluation of registration methods on thoracic CT: The EMPIRE10 challenge. *IEEE Trans Med Imaging* **30**, 1901–20 (2011).
- 522
- 523 42. Baheti, B. *et al.* The brain tumor sequence registration challenge: Establishing correspondence between pre-operative and follow-up MRI scans of diffuse glioma patients. (2021).
- 524
- 525 43. Wang, H. *et al.* Multi-atlas segmentation with joint label fusion. *IEEE Trans Pattern Anal Mach Intell* **35**, 611–23 (2013).
- 526
- 527 44. Tustison, N. J. *et al.* Optimal symmetric multimodal templates and concatenated random forests for supervised brain tumor segmentation (simplified) with ANTsR. *Neuroinformatics* (2014) doi:[10.1007/s12021-014-9245-2](https://doi.org/10.1007/s12021-014-9245-2).
- 528
- 529 45. Tustison, N. J., Yang, Y. & Salerno, M. Advanced normalization tools for cardiac motion correction. in *Statistical atlases and computational models of the heart - imaging and modelling challenges* (eds. Camara, O. et al.) vol. 8896 3–12 (Springer International Publishing, 2015).
- 530

- 531 46. McCormick, M., Liu, X., Jomier, J., Marion, C. & Ibanez, L. ITK: Enabling repro-
532 ducible research and open science. *Front Neuroinform* **8**, 13 (2014).
- 533 47. Kronman, F. A. *et al.* Developmental mouse brain common coordinate framework.
534 **bioRxiv** (2023) doi:[10.1101/2023.09.14.557789](https://doi.org/10.1101/2023.09.14.557789).
- 535 48. Joshi, S. C. & Miller, M. I. Landmark matching via large deformation diffeomor-
536 phisms. *IEEE Trans Image Process* **9**, 1357–70 (2000).
- 537 49. Beg, M. F., Miller, M. I., Trouvé, A. & Younes, L. Computing large deformation
538 metric mappings via geodesic flows of diffeomorphisms. *International Journal of
Computer Vision* **61**, 139–157 (2005).
- 539 50. Avants, B. B. *et al.* The optimal template effect in hippocampus studies of diseased
540 populations. *Neuroimage* **49**, 2457–66 (2010).
- 541 51. Tustison, N. J. *et al.* Optimal symmetric multimodal templates and concatenated
542 random forests for supervised brain tumor segmentation (simplified) with ANTsR.
Neuroinformatics **13**, 209–25 (2015).
- 543 52. Manjón, J. V., Coupé, P., Martí-Bonmatí, L., Collins, D. L. & Robles, M. Adaptive
544 non-local means denoising of MR images with spatially varying noise levels. *J Magn
Reson Imaging* **31**, 192–203 (2010).
- 545 53. Klein, A. *et al.* Evaluation of volume-based and surface-based brain image registration
546 methods. *Neuroimage* **51**, 214–20 (2010).
- 547 54. Tustison, N. J. & Amini, A. A. Biventricular myocardial strains via nonrigid registra-
548 tion of anatomical NURBS model [corrected]. *IEEE Trans Med Imaging* **25**, 94–112
(2006).
- 549 55. Nyúl, L. G., Udupa, J. K. & Zhang, X. New variants of a method of MRI scale
550 standardization. *IEEE Trans Med Imaging* **19**, 143–50 (2000).
- 551 56. Falk, T. *et al.* U-net: Deep learning for cell counting, detection, and morphometry.
552 **Nat Methods** **16**, 67–70 (2019).

- 553 57. Haris, M., Shakhnarovich, G. & Ukita, N. Deep back-projection networks for super-
resolution. in *2018 IEEE/CVF Conference on Computer Vision and Pattern Recog-*
554 *nition* 1664–1673 (2018). doi:[10.1109/CVPR.2018.00179](https://doi.org/10.1109/CVPR.2018.00179).
- 555 58. Avants, B. B. *et al.* Concurrent 3D super resolution on intensity and segmentation
maps improves detection of structural effects in neurodegenerative disease. *medRxiv*
556 (2023) doi:[10.1101/2023.02.02.23285376](https://doi.org/10.1101/2023.02.02.23285376).
- 557 59. Avants, B. B. *et al.* The Insight ToolKit image registration framework. *Front Neu-*
558 *roinform* **8**, 44 (2014).
- 559 60. Tustison, N. J. & Avants, B. B. Explicit B-spline regularization in diffeomorphic image
560 registration. *Front Neuroinform* **7**, 39 (2013).
- 561 61. Avants, B. B. *et al.* A reproducible evaluation of ANTs similarity metric performance
562 in brain image registration. *Neuroimage* **54**, 2033–44 (2011).